Nonreciprocal wide-angle bidirectional absorber based on one-dimensional magnetized gyromagnetic photonic crystals

You-Ming Liu(刘又铭), Yuan-Kun Shi(史源坤), Ban-Fei Wan(万宝飞), Dan Zhang(张丹), and Hai-Feng Zhang(章海锋)

Citation: Chin. Phys. B, 2023, 32 (**4**): 044203. DOI: 10.1088/1674-1056/ac921d
Journal homepage: http://cpb.iphy.ac.cn; http://iopscience.iop.org/cpb

What follows is a list of articles you may be interested in

Angular insensitive nonreciprocal ultrawide band absorption in plasma-embedded photonic crystals designed with improved particle swarm optimization algorithm

Yi-Han Wang(王奕涵) and Hai-Feng Zhang(章海锋)
Chin. Phys. B, 2023, 32 (**4**): 044207. DOI: 10.1088/1674-1056/ac8929

Thermal tunable one-dimensional photonic crystals containing phase change material

Yuanlin Jia(贾渊琳), Peiwen Ren(任佩雯), and Chunzhen Fan(范春珍)†
Chin. Phys. B, 2020, 29 (**10**): 104210. DOI: 10.1088/1674-1056/abab78

Plasmon-phonon coupling in graphene-hyperbolic bilayer heterostructures

Ge Yin(尹格), Jun Yuan(元军), Wei Jiang(姜玮), Jianfei Zhu(朱剑飞), Yungui Ma(马云贵)
Chin. Phys. B, 2016, 25 (**11**): 114216. DOI: 10.1088/1674-1056/25/11/114216

Rectification effect in asymmetric Kerr nonlinear medium

Liu Wan-Guo (刘晚果), Pan Feng-Ming (潘风明), Cai Li-Wei (蔡力伟)
Chin. Phys. B, 2014, 23 (**6**): 064213. DOI: 10.1088/1674-1056/23/6/064213

Optical properties of the electromagnetic waves propagating in an elliptical cylinder multilayer structure

A. Abdoli-Arani
Chin. Phys. B, 2014, 23 (**3**): 034211. DOI: 10.1088/1674-1056/23/3/034211

Nonreciprocal wide-angle bidirectional absorber based on one-dimensional magnetized gyromagnetic photonic crystals

You-Ming Liu(刘又铭)[1], Yuan-Kun Shi(史源坤)[1], Ban-Fei Wan(万宝飞)[1], Dan Zhang(张丹)[2], and Hai-Feng Zhang(章海锋)[1,†]

[1] *College of Electronic and Optical Engineering & College of Flexible Electronics (Future Technology), Nanjing University of Posts and Telecommunications, Nanjing 210023, China*

[2] *College of Information Science and Technology, Nanjing Forestry University, Nanjing* 210037, *China*

(Received 4 July 2022; revised manuscript received 7 September 2022; accepted manuscript online 15 September 2022)

We propose magnetized gyromagnetic photonic crystals (MGPCs) composed of indium antimonide (InSb) and yttrium iron garnet ferrite (YIGF) layers, which possess the properties of nonreciprocal wide-angle bidirectional absorption. Periodical defects in the MGPCs work as filters. Absorption bands (ABs) for the positive and negative propagations arise from the optical Tamm state and resonance in cavities respectively, and they prove to share no overlaps in the studied frequency range. Given $\omega = 2.0138$ THz, for the positive propagation, the ABs in the high-frequency range are localized in the interval between 0.66ω and 0.88ω. In the angular range, the ABs for the TE and TM waves reach 60° and 51°, separately. For the negative propagation, the ABs in the low-frequency range are localized in the interval between 0.13ω and 0.3ω. The ABs extend to 60° for the TE waves and 80.4° for the TM waves. There also exists a narrow frequency band in a lower frequency range. The relevant factors, which include the external temperature, the magnetic fields applied to the YIGF, the refractive index of the impedance matching layer, and the defect thickness, are adjusted to investigate the effects on the ABs. All the numerical simulations are based on the transfer matrix method. This work provides an approach to designs of isolators and so on.

Keywords: nonreciprocal absorption, magnetized gyromagnetic photonic crystals, transfer matrix method, optical Tamm state

PACS: 42.25.Bs, 42.25.–p

DOI: 10.1088/1674-1056/ac921d

1. Introduction

One-dimensional (1D) photonic crystals (PCs), comprising of periodically alternated mediums,[1,2] are often utilized to design optical devices with the properties of nonreciprocity, which have great potential for practical applications,[3] such as isolators,[4,5] circulators,[6,7] and optical diodes.[8–10] Breaking the space-reversal or the time-reversal symmetry of the 1D PCs are two common ways of giving rise to the nonreciprocal properties.[11,12] On the one hand, space-reversal breaking reveals one to adjust the topology of the PCs into asymmetry so that the electromagnetic (EM) waves coupling into the PCs from the two opposite directions go through the energy losses or phase shifts to different degrees. Taken as an example, the quasi-periodic layout is a typical means to enhance nonreciprocity.[13,14] On the other hand, magnetized gyromagnetic photonic crystals (MGPCs),[15–17] kinds of PCs with the introduction of magnetized magneto-optical materials, are capable of realizing time-reversal asymmetry and bringing about nonreciprocal properties. With appropriate structures in the MGPCs, the band gap effects will help to promote nonreciprocity.[18] Many works related to nonreciprocity have been carried out on the basis of the MGPCs. Ardakani[19] proposed a 1-D ternary magnetized plasma PC. It was concluded that the nonreciprocity observed significantly depends on the external magnetic field and the plasma density. Yu *et al.*[20] introduced the defect into the MGPCs and obtained perfect nonreciprocity by optimizing relevant parameters. They owed the unidirectional propagation to the nonreciprocal resonant modes in the magneto-optical medium layers of the proposed structure. Hu *et al.*[21] took advantage of the magneto-optical hyperbolic metamaterials in the MGPCs to realize nonreciprocity and flexible photonic bandgaps, on the basis of the phase variation competition between the magneto-optical material and the general dielectric layers.

Furthermore, absorption plays a significant role in the design of optical cloak,[22] photonic topological insulators,[23] biosensors,[24] and so on. Above all, the introduction of the metal layers can lead to enhancement of absorption, due to the high lossy property.[25–27] In addition, some magneto-optical materials, such as plasmon or indium antimonide (InSb), also have dissipative properties.[28] When frequencies of incident EM waves exceed the plasma frequency of the layers, the energy of the EM waves will be absorbed greatly. What's more, the optical Tamm state (OTS) has attracted the researchers' interest on account of the boost of absorption,[29,30] which in essence can be owed to the resonant property between the interfaces of the layers.

In recent years, some researchers have integrated the

[†]Corresponding author. E-mail: hanlor@163.com or hanlor@njupt.edu.cn

characteristics of nonreciprocity and absorption. However, angular ranges of incident EM waves are not considered. Otherwise, only absorption for the positive or the negative propagation is accomplished, ignorant of absorption for the other propagation. In this study, an MGPC is proposed to realize the nonreciprocal wide-angle bidirectional absorber for the positive and negative propagation. The absorptivity is numerically simulated with the transfer matrix method (TMM) under various incident angle θ and frequency points. Also, the absorption bands (ABs) are defined to be the regime, where the absorptivity is more than 0.9. Δ_{D} is borrowed to describe the nonreciprocity. The magnetized InSb and yttrium iron garnet ferrite (YIGF) layers, the asymmetrical layout of the medium films, and the defect are introduced to result in the nonreciprocity. The influences of the relevant parameters on the ABs are discussed in detail. They include the external temperature, the magnetic fields applied to the YIGF, the refractive index of the impedance matching layer, and the defect thickness. Our results provide a way to design nonreciprocal devices, including optical isolators and so on.

2. Model and theory

As shown in Fig. 1, the designed MGPCs are stratified along the z-direction in the free space. The wave vector k for the incident wave is parallel to the xoz plane with θ indicating the incident angle on the surface of the MGPCs from the outside. The InSb and YIGF layers are exposed to the external magnetic B and H, respectively, both of which are perpendicular to the xoz plane along the positive direction of the y-axis. In the following, B is always set as 1 T.

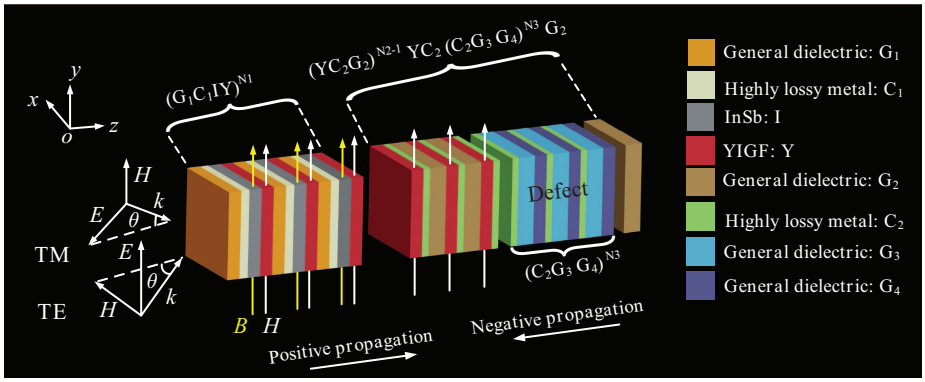

Fig. 1. Schematic of the 1-D MGPCs. The TE and TM waves for the positive and negative propagations are displayed.

The MGPCs consist of two components $\mathrm{MGPC_1}$ and $\mathrm{MGPC_2}$. For simplicity, the $\mathrm{MGPC_1}$ can be written as $(\mathrm{G_1C_1IY})^{N_1}$, where $\mathrm{G_1}$, $\mathrm{C_1}$, I, and Y represent the general dielectric layers, highly lossy metal layers, magnetized InSb, and magnetized YIGF layers, respectively. N_1 stands for the period of the $\mathrm{G_1C_1IY}$ in the $\mathrm{MGPC_1}$, equal to 3. As to the $\mathrm{MGPC_2}$, $\mathrm{C_1}$, $\mathrm{G_2}$, $\mathrm{G_3}$, and $\mathrm{G_4}$ are utilized here to refer to the highly lossy metal layers and general dielectric layers. The $\mathrm{MGPC_2}$ appears in the form of $[(\mathrm{YC_2G_2})^{N_2-1}\ \mathrm{YC_2}\ (\mathrm{C_2G_3\ G_4})^{N_3}\ \mathrm{G_2}]$, where the defect $(\mathrm{C_2G_3\ G_4})^{N_3}$ is introduced into the periodical structure $(\mathrm{YC_2G_2})^{N_2}$ between $\mathrm{C_2}$ and $\mathrm{G_2}$. In the same way, N_1 and N_2 denote the period values, taken as 3 for them. The combination of the $\mathrm{MGPC_1}$ and $\mathrm{MGPC_2}$ brings about the complete MGPC, written as $[(\mathrm{G_1C_1IY})^{N_1}\ (\mathrm{YC_2G_2})^{N_2-1}\ \mathrm{YC_2}\ (\mathrm{C_2G_3\ G_4})^{N_3}\ \mathrm{G_2}]$. Here $d_{\mathrm{G_1}}$, $d_{\mathrm{G_2}}$, $d_{\mathrm{G_3}}$, $d_{\mathrm{G_4}}$, $d_{\mathrm{C_1}}$, and $d_{\mathrm{C_2}}$ are employed to indicate the thicknesses of the general dielectrics $\mathrm{G_1}$, $\mathrm{G_2}$, $\mathrm{G_3}$, and $\mathrm{G_4}$, as well as the thicknesses of the metal layers $\mathrm{C_1}$ and $\mathrm{C_2}$. The specific assignments are as follows: $d_{\mathrm{G_1}} = 5.850\times10^{-5}$ m, $d_{\mathrm{G_2}} = 2.3744\times10^{-3}$ m, $d_{\mathrm{G_3}} = 2.535\times10^{-4}$ m, $d_{\mathrm{G_4}} = 1.090\times10^{-4}$ m, $d_{\mathrm{C_1}} = 2.340\times10^{-5}$ m, and $d_{\mathrm{C_2}} = 6.240\times10^{-6}$ m. In the following study, co is used to quantitatively change the thicknesses of the defect. As a result, the thickness of the defect can be calculated as $d_{\mathrm{f}} = \mathrm{co}\cdot d_{\mathrm{G_4}} + \mathrm{co}\cdot d_{\mathrm{G_3}} + \mathrm{co}\cdot d_{\mathrm{C_2}} = \mathrm{co}\cdot(d_{\mathrm{G_4}} + d_{\mathrm{G_3}} + d_{\mathrm{C_2}})$. In addition, the two magneto-optical mediums YIGF and InSb are sliced into the films with the thicknesses of $d_{\mathrm{Y}} = 6.042\times10^{-5}$ m and $d_{\mathrm{I}} = 1.09\times10^{-4}$ m. The four kinds of the general dielectric $\mathrm{G_1}$, $\mathrm{G_2}$, $\mathrm{G_3}$, and $\mathrm{G_4}$ are composite materials, whose refractive indexes $n_{\mathrm{G_1}}$, $n_{\mathrm{G_2}}$, $n_{\mathrm{G_3}}$, and $n_{\mathrm{G_4}}$ are 4, 1.2, 1.2, and 2.8, respectively. The highly lossy metals $\mathrm{C_1}$ and $\mathrm{C_2}$ are a kind of the artificially compounded material, with the refractive index set as $7.63 + \mathrm{j}6.39$.

The TMM is taken as the method of simulation. As the isotropic materials, the matrix is given by[31,32]

$$\boldsymbol{M}_i = \begin{pmatrix} \cos(k_{iz}d_i) & -\frac{\mathrm{j}}{\eta_i}\sin(k_{iz}d_i) \\ -\mathrm{j}\eta_i\sin(k_{iz}d_i) & \cos(k_{iz}d_i) \end{pmatrix}, \tag{1}$$

where $i = \mathrm{G_1}$, $\mathrm{G_2}$, $\mathrm{G_3}$, $\mathrm{G_4}$, $\mathrm{C_1}$, and $\mathrm{C_2}$; k_{iz} is the z component of the incident wave vector. For the TE and TM waves, $\eta_i = \sqrt{\varepsilon_0/\mu_0}\cdot n_i\cdot\cos\theta_i$ and $\eta_i = \sqrt{\varepsilon_0/\mu_0}\cdot n_i/\cos\theta_i$, respectively, and θ_i represents the incident angles on the surface of the i layers.

The Y and I are classified into magneto-optical mediums. The permeability and permittivity of the mediums may rep-

resent the form of the tensors with different kinds of waves permeated in them.

Considering the Y layers initially, the Y layers' permittivity maintains the constant $\varepsilon_{\rm f} = 15$.[33] For TM waves, the effective refractive index is written as[33]

$$n_{\rm Y(TM)} = \sqrt{\varepsilon_{\rm f} \cdot \mu_0}. \tag{2}$$

However, in the case of TE waves, the permeability of the Y layers exhibits anisotropical behavior, and its tensor can be rewritten as[34]

$$\boldsymbol{\mu}_{\rm Y} = \begin{pmatrix} \mu_{\rm r} & 0 & {\rm j}\mu_{\rm k} \\ 0 & \mu_0 & 0 \\ -{\rm j}\mu_{\rm k} & 0 & \mu_{\rm r} \end{pmatrix}. \tag{3}$$

The relative functions can be written as[33]

$$\mu_{\rm r} = 1 + \frac{\omega_{\rm m}(\omega_{01} - {\rm j}\gamma\omega)}{(\omega_{01} - {\rm j}\gamma\omega)^2 - \omega^2}, \tag{4}$$

$$\mu_{\rm k} = \frac{\omega_{\rm m}\omega}{(\omega_{0_1} - {\rm j}\gamma\omega)^2 - \omega^2}, \tag{5}$$

where ω is the angular frequency, $\omega_{\rm m}$ is the circular frequency equal to $2\pi \times 2.8 \times 10^6 \times M_{\rm s}$,[33] and $\omega_{01} = 2\pi \times 2.8 \times 10^6 \times H$[33] is the resonance frequency. The saturation magnetization $M_{\rm s}$ and the damping constant γ are 1780 Oe and 0.0002, respectively.[33]

Then the effective permeability of the Y layers is worked out as[33]

$$\mu_{\rm eff} = \left(\mu_{\rm r}^2 + ({\rm j}\mu_{\rm k})^2\right)/\mu_{\rm r}. \tag{6}$$

Given the Y layer's permittivity $\varepsilon_{\rm f} = 15$, one can obtain the effective refractive index[33]

$$n_{\rm Y(TE)} = \sqrt{\varepsilon_{\rm f}\left(\mu_{\rm r}^2 + ({\rm j}\mu_{\rm k})^2\right)/\mu_{\rm r}}. \tag{7}$$

Finally, the transfer matrices of the Y layers under the TE waves and TM waves can derived as follows:

$$\boldsymbol{M}_{\rm Y(TE)} = \begin{pmatrix} \cos(k_{\rm Yz(TE)}d_{\rm Y}) - \frac{k_{\rm Yx(TE)}\mu_{\rm k}}{k_{\rm Yz(TE)}\mu_{\rm r}}\sin(k_{\rm Yz(TE)}d_{\rm Y}) & {\rm j}\eta_{\rm Y(TE)}\sin(k_{\rm Yz(TE)}d_{\rm Y}) \\ \frac{\rm j}{\eta_{\rm Y(TE)}}\left[1 + \left(\frac{k_{\rm Yx(TE)}\mu_{\rm k}}{k_{\rm Yz(TE)}\mu_{\rm r}}\right)^2\right]\sin(k_{\rm Yz(TE)}d_{\rm Y}) & \cos(k_{\rm Yz(TE)}d_{\rm Y}) + \frac{k_{\rm Yx(TE)}\mu_{\rm k}}{k_{\rm Yz(TE)}\mu_{\rm r}}\sin(k_{\rm Yz(TE)}d_{\rm Y}) \end{pmatrix}, \tag{8}$$

$$\boldsymbol{M}_{\rm Y(TM)} = \begin{pmatrix} \cos(k_{\rm Yz(TM)}d_{\rm Y}) & -\frac{\rm j}{\eta_{\rm Y(TM)}}\sin(k_{\rm Yz(TM)}d_{\rm Y}) \\ -{\rm j}\eta_{\rm Y(TM)}\sin(k_{\rm Yz(TM)}d_{\rm Y}) & \cos(k_{\rm Yz(TM)}d_{\rm Y}) \end{pmatrix}. \tag{9}$$

For TE waves, $\eta_{\rm Y(TE)} = \sqrt{\varepsilon_{\rm f}\left(\mu_{\rm r}^2 + ({\rm j}\mu_{\rm k})^2\right)/\mu_{\rm r}}/\cos(\theta_{\rm Y})$. The wave vectors are decomposed in quadrature as $k_{\rm Yz(TE)} = n_{\rm Y(TE)} \cdot \cos\theta_{\rm Y} \cdot \omega/c$ and $k_{\rm Yx(TE)} = n_{\rm Y(TE)} \cdot \sin\theta_{\rm Y} \cdot \omega/c$, in which c is the velocity of light in vacuum. For the TM waves, $\eta_{\rm Y(TM)} = \sqrt{\varepsilon_{\rm f}\varepsilon_0}/[\mu_0\cos(\theta_{\rm Y})]$. The wave vector along the z-axis can be written as $k_{\rm Yz(TM)} = n_{\rm Y(TM)} \cdot \cos\theta_{\rm Y} \cdot \omega/c$. Here, $\theta_{\rm Y}$ is the incident angle on the surface of the Y layers.

When it comes to the I layers, for TE waves, the permittivity is described by the Drude model[35,36]

$$\varepsilon_{\rm I(TE)} = \varepsilon_\infty - \omega_{\rm p}^2/\left(\omega^2 + {\rm j}\nu_{\rm c}\omega\right), \tag{10}$$

where $\varepsilon_\infty = 15.68$[35,36] is the high-frequency limit permittivity and $\nu_{\rm c}$ is the collision frequency of carriers, taken as 0.1π THz;[36] $\omega_{\rm p}$ is plasma frequency, the function of which is expressed as $(Ne^2/\varepsilon_0 m^*)^{1/2}$;[35–37] e, ε_0 and m^* are the electron charge, the permittivity in the vacuum and the effective mass of the carrier. With regard to the I layers, $m^* = 0.15m_{\rm e}$ and $m_{\rm e}$ is the mass of an electron. What's more, $\omega_{\rm p}$ largely depends on the intrinsic carrier density N, relevant to the temperature T_0. N can be written as[35–37]

$$N({\rm m}^{-3}) = 5.76 \times 10^{20} T_0^{1.5} \times \exp[-0.26/(2 \times 8.625 \times 10^{-5} \times T_0)]. \tag{11}$$

Supposing that the relative permeability is 1, then, the effective refractive index for the TE wave is expressed as

$$n_{\rm I(TE)} = \sqrt{\varepsilon_{\rm I(TE)}}. \tag{12}$$

In terms of TM waves, the permittivity of the I layers likewise is in the form of the tensor expressed as[36]

$$\varepsilon_{\rm I} = \begin{pmatrix} \varepsilon_x & 0 & {\rm j}\varepsilon_{xz} \\ 0 & \varepsilon_y & 0 \\ -{\rm j}\varepsilon_{xz} & 0 & \varepsilon_x \end{pmatrix}, \tag{13}$$

where

$$\varepsilon_x = \varepsilon_\infty - \varepsilon_\infty \frac{\omega_{\rm p}^2(\omega + {\rm j}\nu_{\rm c})}{\omega\left[(\omega + {\rm j}\nu_{\rm c})^2 - \omega_{\rm c}^2\right]}, \tag{14}$$

$$\varepsilon_y = \varepsilon_\infty - \varepsilon_\infty \frac{\omega_{\rm p}^2}{\omega(\omega + {\rm j}\nu_{\rm c})}, \tag{15}$$

$$\varepsilon_{xz} = \varepsilon_\infty \frac{\omega_{\rm p}^2\omega_{\rm c}}{\omega\left[(\omega + {\rm j}\nu_{\rm c})^2 - \omega_{\rm c}^2\right]}. \tag{16}$$

Apart from ε_∞ and $\omega_{\rm p}$, which have been demonstrated ahead, the cyclotron frequency $\omega_{\rm c}$ is proportional to the external electric field by $\omega_{\rm c} = eB/m^*$. The effective refractive index for the TM waves can be obtained as follows:[36]

$$n_{\mathrm{I(TM)}} = \sqrt{\varepsilon_{\mathrm{TM}}} = \sqrt{\frac{\varepsilon_x^2 - \varepsilon_{xz}^2}{\varepsilon_x}}. \tag{17}$$

Lastly, the transfer matrices of the I layers for the TM and TE waves can be deduced as follows:

$$\boldsymbol{M}_{\mathrm{I(TM)}} = \begin{pmatrix} \cos(k_{\mathrm{Iz(TM)}}d_{\mathrm{I}}) + \frac{k_{\mathrm{Ix(TM)}}\varepsilon_{xz}}{k_{\mathrm{Iz(TM)}}\varepsilon_x}\sin(k_{\mathrm{Iz(TM)}}d_{\mathrm{I}}) & -\frac{\mathrm{j}}{\eta_{\mathrm{I(TM)}}}\left[1+\left(\frac{k_{\mathrm{Ix(TM)}}\varepsilon_{xz}}{k_{\mathrm{Iz(TM)}}\varepsilon_x}\right)^2\right]\sin(k_{\mathrm{Iz(TM)}}d_{\mathrm{I}}) \\ -\mathrm{j}\eta_{\mathrm{I(TM)}}\sin(k_{\mathrm{Iz(TM)}}d_{\mathrm{I}}) & \cos(k_{\mathrm{I(TMz)}}d_{\mathrm{I}}) - \frac{k_{\mathrm{Ix(TM)}}\varepsilon_{xz}}{k_{\mathrm{Iz(TM)}}\varepsilon_x}\sin(k_{\mathrm{Iz(TM)}}d_{\mathrm{I}}) \end{pmatrix}, \tag{18}$$

$$\boldsymbol{M}_{\mathrm{I(TE)}} = \begin{pmatrix} \cos(k_{\mathrm{I(TEz)}}d_{\mathrm{I}}) & -\frac{\mathrm{j}}{\eta_{\mathrm{I(TE)}}}\sin(k_{\mathrm{I(TEz)}}d_{\mathrm{I}}) \\ -\mathrm{j}\eta_{\mathrm{I(TE)}}\sin(k_{\mathrm{I(TEz)}}d_{\mathrm{I}}) & \cos(k_{\mathrm{I(TEz)}}d_{\mathrm{I}}) \end{pmatrix}. \tag{19}$$

Similarly, θ_{I} denotes the incident angle on the I layers; $\eta_{\mathrm{I(TM)}} = \sqrt{\varepsilon_0/\mu_0}n_{\mathrm{I(TM)}}/\cos(\theta_{\mathrm{I}})$ in the case of the TM waves; $k_{\mathrm{Iz(TM)}}$ and $k_{\mathrm{Ix(TM)}}$ are the decompositions of the incident waves in the orthogonal directions, in which $k_{\mathrm{Iz(TM)}} = n_{\mathrm{I(TM)}}\cdot\cos(\theta_{\mathrm{I}})\cdot\omega/c$ and $k_{\mathrm{Ix(TM)}} = n_{\mathrm{I(TM)}}\cdot\sin(\theta_{\mathrm{I}})\cdot\omega/c$. Also, $\eta_{\mathrm{I(TM)}} = \sqrt{\varepsilon_0/\mu_0}n_{\mathrm{I(TM)}}\cdot\cos(\theta_{\mathrm{I}})$, when it comes to the TE waves; $k_{\mathrm{Iz(TM)}} = n_{\mathrm{I(TM)}}\cdot\cos\theta_{\mathrm{I}}\cdot\omega/c$ refers to the component of the incident waves in the z-direction.

The total transfer matrix $\boldsymbol{M}$ builds up a bridge between the incident EM field $(E_1, H_1)^{\mathrm{T}}$ and the emergent EM field $(E_{N+1}, H_{N+1})^{\mathrm{T}}$ through the whole structure. $\boldsymbol{M}$ reads

$$\begin{pmatrix} E_1 \\ H_1 \end{pmatrix} = \begin{pmatrix} M_{11} & M_{12} \\ M_{21} & M_{22} \end{pmatrix}\begin{pmatrix} E_{N+1} \\ H_{N+1} \end{pmatrix} = \boldsymbol{M}\begin{pmatrix} E_{N+1} \\ H_{N+1} \end{pmatrix}. \tag{20}$$

The transfer matrix for the positive propagation is derived as follows:

$$\begin{aligned} M_{\mathrm{positive}} = {} & (M_{\mathrm{G_1}}M_{\mathrm{C_1}}M_{\mathrm{I}}M_{\mathrm{Y}})^3(M_{\mathrm{Y}}M_{\mathrm{C_2}}M_{\mathrm{G_2}})^2 \\ & \cdot M_{\mathrm{Y}}M_{\mathrm{C_2}}(M_{\mathrm{C_2}}M_{\mathrm{G_3}}M_{\mathrm{G_4}})^3 M_{G_2}. \end{aligned} \tag{21}$$

The transfer matrix for the negative propagation can be attained in the same way:

$$\begin{aligned} M_{\mathrm{negative}} = {} & M_{\mathrm{G_2}}(M_{G_4}M_{\mathrm{G_3}}M_{\mathrm{C_2}})^3 M_{\mathrm{C_2}} \\ & \cdot M_{\mathrm{Y}}(M_{\mathrm{G_2}}M_{\mathrm{C_2}}M_{\mathrm{Y}})^2(M_{\mathrm{Y}}M_{\mathrm{I}}M_{\mathrm{C_1}}M_{\mathrm{G_1}})^3. \end{aligned} \tag{22}$$

The reflectivity R and transmissivity T are calculated as follows:

$$R = |r|^2, \tag{23}$$

$$T = |t|^2, \tag{24}$$

where

$$r = \frac{M_{11}\eta_0 + M_{12}\eta_0\eta_{N+1} - M_{21} - M_{22}\eta_{N+1}}{M_{11}\eta_0 + M_{12}\eta_0\eta_{N+1} + M_{21} + M_{22}\eta_{N+1}}, \tag{25}$$

$$t = \frac{2\eta_0}{M_{11}\eta_0 + M_{12}\eta_0\eta_{N+1} + M_{21} + M_{22}\eta_{N+1}}. \tag{26}$$

According to the conservation of energy, absorptivity A can be inferred as follows:

$$A = 1 - R - T. \tag{27}$$

Because the MGPCs are lain in free space, η and η_{N+1} are equal to η_{air}. In the event of the TE waves, $\eta_{\mathrm{air}} = \sqrt{\varepsilon_0/\mu_0}n_{\mathrm{air}}/\cos(\theta_{\mathrm{air}})$, as well as $\eta_{\mathrm{air}} = \sqrt{\varepsilon_0/\mu_0}n_{\mathrm{air}}\cdot\cos(\theta_{\mathrm{air}})$ for the TM waves, with θ_{air} indicating the incident angle.

Furthermore, to describe the nonreciprocity, Δ_{D} is defined to demonstrate the properties of the nonreciprocal absorption,

$$\Delta_{\mathrm{D}} = |A_{\mathrm{positive}} - A_{\mathrm{negative}}|. \tag{28}$$

3. Discussion

Here, the angular frequency $\omega = 2.0138$ THz is utilized to normalize the studiec regimes and ω remains constant in the following. Figure 2 demonstrates the individual curves in the case of the normal incidence by taking co $= 1$, $T = 295$ K, and $H = 10000$ Oe. When it comes to the TE waves, the absorptivity over 0.9 ranges from 0.66ω to 0.88ω for the positive propagation, while for the negative propagation it is from $0.19\omega_0$ to 0.3ω mainly, as well as an extra band in the lower frequency between $0.078\omega_0$ and 0.097ω. In regards of the TM waves, the absorption interval for the positive propagation is narrowed between 0.69ω and 0.85ω. However, the range for the negative propagation is expanded, covering from $0.13\omega_0$ to 0.3ω, as well as the extra low-frequency absorption band extending from $0.059\omega_0$ to 0.082ω. The frequency range for the positive and the negative propagations reveals a distinct nonreciprocity, in which the parallel frequency range for the other propagation is exactly in the state of low absorptivity as the absorptivity maintains a relatively high value over a frequency range for the positive or negative propagation. In fact, in the studied range, the transmission is negligible and the incident waves are either absorbed or reflected. Figures 2(b) and 2(e) demonstrate the phenomenon explicitly. For example, the reflectivity for the positive propagation in Fig. 2(b) compensates for the absorptivity in the positive propagation shown in Fig. 2(a), both of them can sum up to one.

The higher the value of Δ_{D}, the better the unidirectional absorption property. Corresponding to the frequency bands, where the absorptivity exceeds 0.9 for both kinds of propagation, the spectra of the Δ_{D} are above the standard line 0.9

approximately and share similar trends, indicating the nonreciprocal bidirectional absorption of the MGPCs.

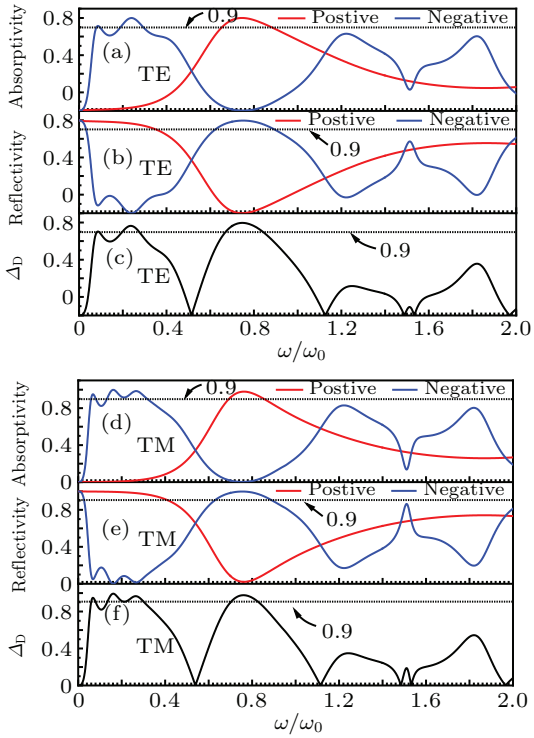

Fig. 2. Given $\theta = 0°$ and the incident TE waves, (a) the absorptivity spectra with the red one for the positive propagation and the blue one for the negative propagation, (b) the reflectivity spectra with the red one for the positive propagation and the blue one for the negative propagation, and (c) the Δ_D for the TE waves of $\theta = 0°$. Given $\theta = 0°$ and the incident TM waves, (d) the absorptivity spectra with the red one for the positive propagation and the blue one for the negative propagation, (e) the reflectivity spectra with the red one for the positive propagation and the blue one for the negative propagation, and (f) the Δ_D for the TE waves of $\theta = 0°$.

With the varying incident angles, Fig. 3 exhibits the ABs and reflectivity for the positive and negative propagations, as well as the Δ_D. For the positive propagation, Fig. 3(a) exhibits that the AB of the TE wave is broader and insensitive to the angle changes, compared to the AB of the TM wave in general. The former extends to 60° approximately, while the latter covers the range from 0° to 51°. The widest absorption frequency ranges are both at $\theta = 0°$. For the negative propagation, Fig. 3(b) illustrates the exactly opposite phenomena. The AB of the TM waves proves to be broader, and overrides a wider angular range, reaching 80.4°. Yet, the AB of the TE waves keeps extending to a higher incident angle and stops at 60°. The AB of the TE waves turns out to be the widest at 0° and the width of AB of the TM waves attains its maximum at 62°, holding the range of 0.46ω. It is well worth noticing that for the negative propagation, there exists an additional narrow AB in the lower frequency regime in Fig. 3(b). It covers a width no more than 0.04ω, and extends horizontally to 71.2° in the case of the TE waves, but is merged into the main AB over the TM waves regime at $\theta = 51°$. Figures 3(c) and 3(d) demonstrate that the regimes of the low absorptivity are occupied with the high reflectivity. For the positive propagation, the band gap shares a considerable frequency range and angular range with the AB for the negative propagation. The band gap for the positive propagation and the AB for the negative propagation hold an overlap in the frequency range and the angular range.

Δ_D shown in Fig. 3(e) will prove the nonreciprocity more clearly. In general, the ABs for the negative and the positive propagation are perfectly staggered. However, the larger the angle is, the worse the absorption property tends to be. Compared to the AB for the positive propagation, over the parallel band, the angular range of Δ_D over 0.9 remains almost unchanged in the TE wave regime, while it shrinks to 41° as for the TM waves. Similarly, when it comes to the Δ_D in the corresponding frequency range for the negative propagation, the regime of Δ_D over 0.9 is narrowed down. It extends from 0° to 57° in the case of the TE waves, and the range is between 0° and 79.6° for the TM waves.

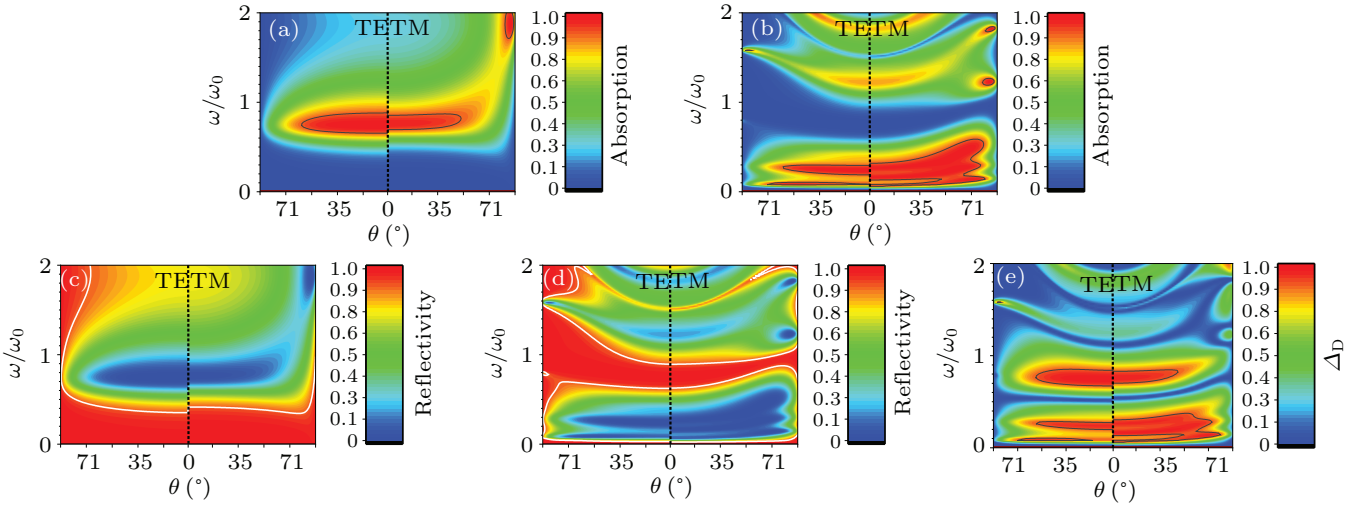

Fig. 3. Contour maps illustrating (a) AB for the positive propagation, and (b) AB for the negative propagation. The solid black lines enclose the regimes of the absorptivity greater than 0.9. [(d), (e)] The reflectivity for the positive and negative propagation, respectively. The reflectivity is 0.9 on the white lines. The band of Δ_D is given in (e).

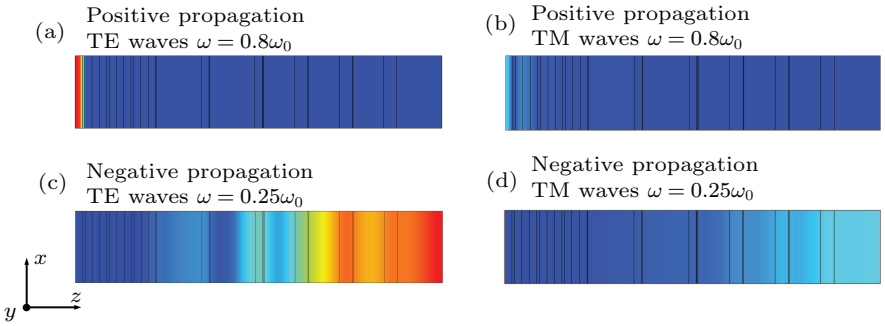

Fig. 4. Supposing $\theta = 0°$, the simulated distributions of the electric field norms under the two frequency points and modes for the positive and the negative propagation. (a) The TE waves under 0.8ω for the positive propagation, (b) the TM waves under 0.8ω for the negative propagation, (c) the TE waves under 0.25ω for the positive propagation, and (d) the TM waves under 0.8ω for the negative propagation. Various colors mark the strength of the electric norms.

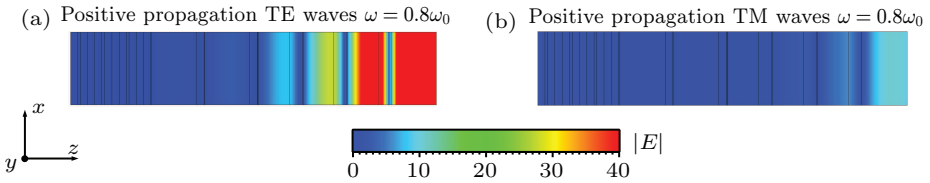

Fig. 5. Supposing $\theta = 0°$ and $\omega = 0.8\omega$, the simulated distributions of the electric field norms under TE and TM modes for the negative propagation. (a) The TE waves under 0.8ω, (b) the TM waves under 0.8ω. Various colors mark the strength of the electric norms.

To explore the mechanism of the absorption, the distributions of the electric field norms are presented in Fig. 4. The selected frequency points of the incident EM waves are 0.8ω for the positive propagation and 0.25ω for the negative propagation in the absorbable frequency band. No matter whether the incident EM waves are the TE or TM waves, for the positive propagation, the amplitudes of the electric fields are strong around the C_1 layers, while the energy turns out relatively weak in the C_1 media layer. In addition, the amplitudes of the electric field norms decay through the MGPC. It can be attributed to the OTS. Lain behind the high loss metal layers C_1, the units of the Y and I layers function as the optical mirrors, blocking the EM waves in the specific frequency range. Then due to the strong impedance of the metal layers, hardly can the EM waves go through the C_1 layers as well. As a result, the EM waves resonate between the C_1 layers and the units, thus concentrating the EM fields around the interfaces right there. What's more, considering the great impedance between the metal layers and the free space, in each period of the $(G_1C_1IY)^{N_1}$, the dielectric layers G_1 are designed in place to couple to the EM waves before the C_1 layers, so that the EM waves will couple into the structure easily, helping to enhance the absorption. It can also be concluded from Fig. 4 that the absorption of the TE waves seems more efficient than the electric fields that are nearly consumed in the first period of the $MGPC_1$, while the TM waves penetrate through the first period and nearly decay out in the second period.

The periodical structure $(G_2C_2Y)^{N_2}$ and the defect $(G_4G_3C_2)^{N_3}$ are dedicated to the AB for the negative propagation, equally. Instead of being localized around some layers, the energy of the electric fields is weakened gradually through the whole structure and, in particular, it is worn out visibly in the G_2 layers and G_3 layers. In the defect, the G_3 layers work like cavities, along with the G_4 and C_2 layers acting as the reflecting barriers, which leads to the coherent subtraction in the cavities. So is the same with the $(G_2C_2Y)^{N_2}$. Except for the first period of the $(G_2C_2Y)^{N_2}$, the G_2 layers play the role of the cavities between the reflecting barriers of the C_2 and Y layers. From Figs. 4(c) and 4(d), it comes that the TM waves are more easily absorbed than the TE waves.

What's more about the defect, apart from the contribution to the absorption, the defect also performs the effects of filtering. The units of the G_4 and G_3 in the defect will prevent the permeation of some EM waves into the structure. As a result, in the corresponding frequency range, the absorptivity can be reduced to nearly zero. Figure 5 exhibits the distributions of the electric field norms under TE and TM modes for the negative propagation. As is shown, in the case of $\omega = 0.8\omega$, very weak energy can pass through the defective layer into the MGPC deeply.

The properties of the I layers are related to the external conditions. The effects of T_0 on nonreciprocal ABs are displayed in Fig. 6, which reveals the nonreciprocal phenomenon compelled by $T_0 = 335$ K, 295 K, 255 K, and 215 K. H and co are chosen to be 10000 Oe and 1. It is apparent that T_0 has no effects on the ABs for the negative propagation. The coming discussion focuses on the ABs for positive propagation. The decrease of T_0 shrinks the ABs in the scale of the angular range and expands them to the frequency range. In respect of the TE waves, there is little difference when T_0 is 335 K and 295 K and the ABs reach 63.4° and 60°, respectively. As the temperature drops to $T_0 = 255$ K, the angular width ranges from 0° to

52.6°. In the case of $T_0 = 335$ K, 295 K, and 255 K, the bandwidth of the AB is widest at 0° and mounts up uniformly from 0.18ω to 0.22ω and 0.24ω with the decreasing T_0. $T_0 = 215$ K narrows the angular range down to 33.4°, but swells the frequency range to 0.36ω. When it comes to the TM waves, the same is true for the trends of the ABs. As T_0 decreases, the width of the AB at its maximum runs from 0.23ω to 0.16ω. The ABs of $T_0 = 255$ K and 295 K share a same frequency range as 0.17ω. As to the angular range, the AB reaches 60° at $T_0 = 215$ K but is retreated to 49.2° at $T_0 = 335$ K.

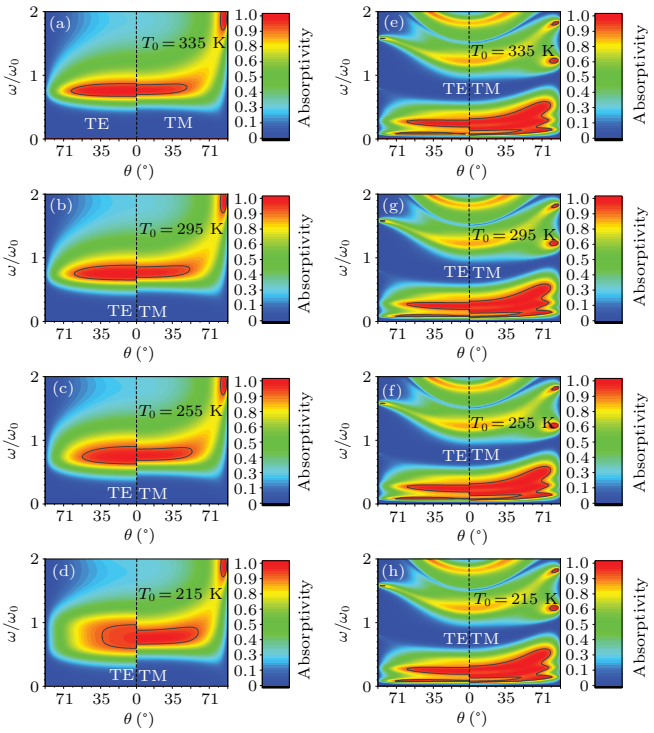

Fig. 6. Contour maps illustrating the ABs of (a) $T_0 = 335$ K for the positive propagation, (b) $T_0 = 295$ K for the positive propagation, (c) $T_0 = 255$ K for the positive propagation, (d) $T_0 = 215$ K for the positive propagation, (e) $T_0 = 335$ K for the negative propagation, (f) $T_0 = 295$ K for the negative propagation, (g) $T_0 = 255$ K for the negative propagation, and (h) $T_0 = 215$ K for the negative propagation. Various colors mark the different values with diverse frequency points and θ_s. The solid black lines enclose the regimes of the absorptivity more than 0.9.

The effective refractive index of the Y layers is modulated by H. As shown in Fig. 7, providing $T_0 = 295$ K and co = 1, H is regulated as 10000 Oe, 1000 Oe, and 100 Oe. The varying H makes no difference to the ABs for the positive propagation but has certain effects on the ABs of the TM waves for the negative propagation. When H is adjusted from 10000 Oe to 1000 Oe, the high-frequency ABs are not influenced in either the angular range or the frequency range. But the narrow band in the low frequency is limited between 26.8° and 72.6° in the angular range for the TE waves. As H is reduced to 100 Oe, the narrow band in the low frequency disappears completely, but here comes the expansion of the AB in the high-frequency range. For $\theta = 0°$, the upper edge of the AB maintain at 0.3ω, but the lower edge of the AB comes down to 0.12ω, covering a frequency range of 0.18ω. Apparently, it is hard to adjust the ABs for the positive propagation by various H. On basis of the OTS as denoted before, the optical mirrors, comprising of the Y and I layers, play the significant role in localizing the EM fields around the metal C_1 layers. However, the responses of the Y layers to the changing H are weak in the corresponding study band. As a result, the effects of H on the ABs is feeble.

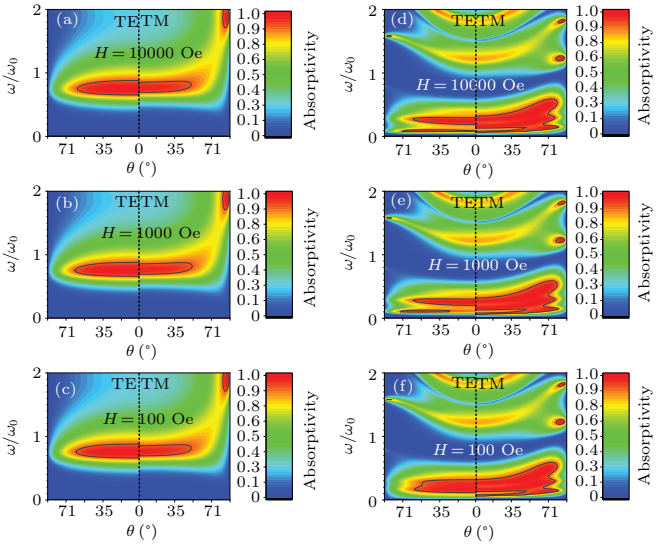

Fig. 7. Contour maps illustrating the ABs of (a) $H = 10000$ Oe for the positive propagation, (b) $H = 1000$ Oe for the positive propagation, (c) $H = 100$ Oe for the positive propagation, (d) $H = 10000$ Oe for the negative propagation, (e) $H = 1000$ Oe for the negative propagation, (f) $H = 100$ Oe for the negative propagation. Various colors mark the different values with diverse frequency points and θ_s. The solid black lines enclose the regimes of the absorptivity more than 0.9.

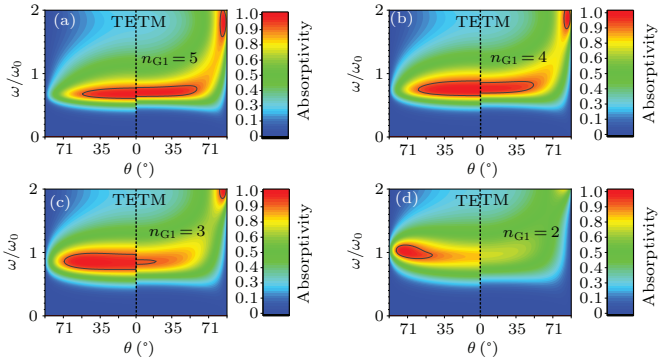

Fig. 8. Contour maps illustrating the ABs for the positive propagation of (a) $n_{G_1} = 5$, (b) $n_{G_1} = 4$, (c) $n_{G_1} = 3$, and (d) $n_{G_1} = 2$. Various colors mark the different values with diverse frequency points and θ_s. The solid black lines enclose the regimes of the absorptivity more than 0.9.

In the design, the G_1 layers, working as the impedance matching layers, help to enhance the absorption. As shown in Fig. 8, given co = 1, $H = 10000$ Oe, and $T_0 = 295$ K, the refractive index is adjusted to study the responses of the ABs to the positive propagation. The ABs of $n_{G_1} = 5$ and $n_{G_1} = 4$ are relatively broad in the scale of the frequency range and the angular range. For the AB of $n_{G_1} = 5$, the TE waves hold a wider frequency range such that, at $\theta = 0°$, the width of the AB covers 0.14ω. However, the angular range is narrower than that of the TM waves, whose angular range reaches 59.4°. In the

case of $n_{G_1} = 3$, the angular range of the TE waves is greatly expanded, where the band becomes as far as $\theta = 69.8°$. As to the frequency range, at $\theta = 0°$, it shifts to a higher frequency between 0.72ω and 0.96ω. The AB of $n_{G_1} = 3$ is insensitive to the increasing θ and the width is maintained at 0.24ω over a wide angular range between $\theta = 0°$ and $\theta = 51°$. Turning to the AB of the TM waves, $n_{G_1} = 3$ greatly tightens the angular range and frequency range, the angular range is limited between $\theta = 0°$ and $\theta = 14.4°$. The AB of the TM waves evaporates as $n_{G_1} = 2$. The AB of the TE waves is demarcated from $\theta = 47.8°$ to $\theta = 81.8°$ in the angular range.

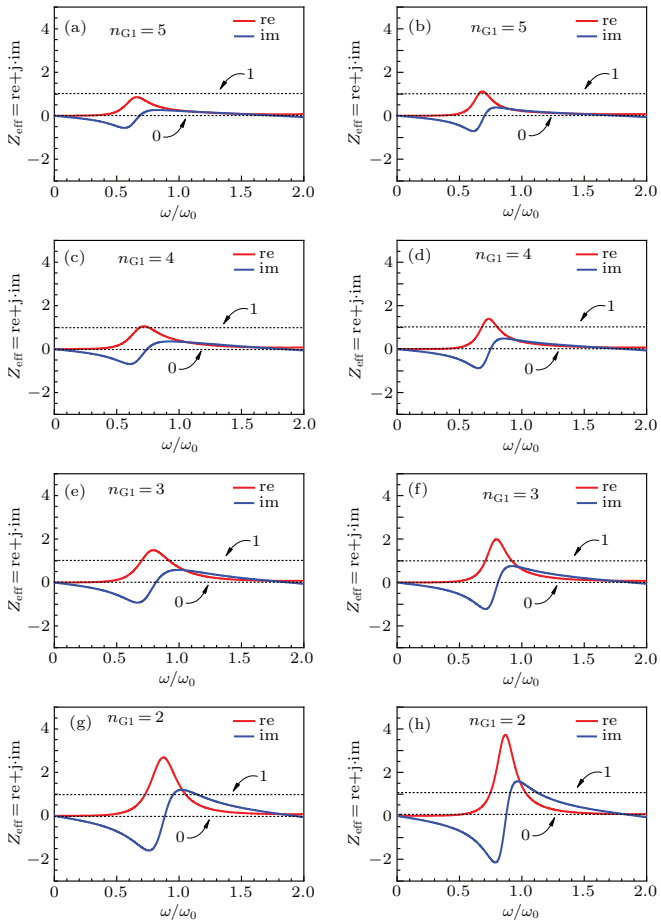

Fig. 9. The spectra of the effective normalized impedance under different polarization modes and varying n_{G_1} when $\theta = 0°$. (a) TE mode with $n_{G_1} = 5$, (b) TM mode with $n_{G_1} = 5$, (c) TE mode with $n_{G_1} = 4$, (d) TM mode with $n_{G_1} = 4$, (e) TE mode with $n_{G_1} = 3$, (f) TM mode with $n_{G_1} = 3$, (g) TE mode with $n_{G_1} = 2$, and (h) TM mode with $n_{G_1} = 2$. The red and blue curves indicate the real and imaginary parts, respectively.

Taking $\theta = 0°$, the impedance spectra of the MGPCs are depicted in Fig. 9 to explain the phenomena of different ABs with diverse n_{G_1}. The effective normalized impedance of the MGPCs is relevant to the reflection coefficient r, written as[38]

$$\frac{Z_{\text{eff}}}{Z_0} = \text{re} + \text{j} \cdot \text{im} = \frac{1+r}{1-r}, \tag{29}$$

where $Z_0 \approx 377\ \Omega$ represents the impedance in the vacuum and Z_{eff} denotes the effective impedance of the MGPCs. The perfect impedance matching can be briefly and mathematically summarized as the following conditions: the reactance (im) equates to zero and the resistance (re) is equivalent to one, in which there will be no reflection and the EM waves will couple into the MGPCs entirely. It is of benefit for the subsequent absorption in the structure to ensure that most of the EM waves can enter the MGPCs. Regardless of the kind of the modes, in the case of $n_{G_1} = 4$ and 5, the value of re is around one and im displays an increasing trend and smoothly floats over the standard dot line of zero, over the corresponding frequency range of the ABs. It almost meets with the impedance matching, meaning that most of the EM waves go through the surface of the MGPCs with ignorant reflection. Turning to the spectra of $n_{G_1} = 2$ and 3 in Figs. 9(e)–9(h), in the parallel frequency range, apart from the TE waves of $n_{G_1} = 3$, the difference between one and re becomes larger, despite the im still around the dotted line of zero. The weakening for the EM to couple into the MGPCs verifies the weakening absorptivity in the case of $n_{G_1} = 2$ and 3.

The defect plays a significant role in the ABs for the negative propagation. To investigate the influences of the defect thickness on the ABs, the co is valued as 0.5, 1, 1.5, and 2, providing $T_0 = 295$ K and $H = 10000$ Oe. As illustrated in Fig. 10, the smaller the co is, the wider the AB is prone to be. Compared to the AB of co = 1, the AB of co = 0.5 shifts to a higher frequency range and it holds a width of 0.42ω for the TE waves and 0.5ω for the TM waves at $\theta = 0°$. As to the TE waves, the AB reaches as far as 85.4°, while it attains 78.2° for the TM waves. With respect to the AB of co = 1.5, it is apparent that the band where the absorptivity approaches zero is located in a relatively lower frequency range than that of co = 1. Here co = 1.5 compresses the AB even more narrowly. When the TM waves incident at $\theta = 70.6°$ the width of the AB reaches its peak around $0.24\omega_0$ merely.

Considering $T_0 = 295$ K, co = 1 and $H = 10000$ Oe, Fig. 11 displays the ABs under the circumstance with the defect located between different interlayers. In the case of $[(G_1C_1IY)^{N_1}\ (YC_2G_2)^{N_2}\ (C_2G_3\ G_4)^{N_3}]$, the angular range of the ABs does not change much compared to that given in Fig. 11(b) with the structure in the form of $[(G_1C_1IY)^{N_1}\ (YC_2G_2)^{N_2-1}\ YC_2\ (C_2G_3\ G_4)^{N_3}\ G_2]$. As illustrated in Fig. 11(b), in the TM wave regime, the AB reaches 80.4°, as well as the AB attains 60° in the case of the TE waves. As to the narrow AB in the lower frequency range, it ranges from 0° to 71.2° in the TE wave regime. When it comes to Fig. 11(a), the AB covers the range from 0° to 79.8° in the TM wave domain, while the edge of the AB shrinks down to 59° in the TE wave regime. In addition, the narrow AB in the low wave range reaches 70.4° in the TE wave regime. In terms of the frequency range, the location of the defect makes little difference from the ABs in Fig. 11(b). Supposing the normal incident TM wave, the AB is $0.17\omega_0$ in width.

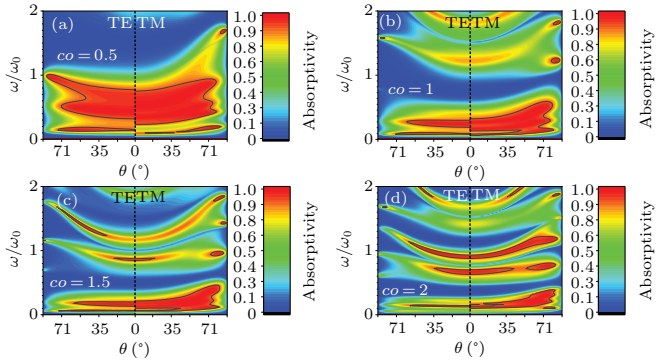

Fig. 10. Contour maps illustrating the ABs for the negative propagation of (a) co = 0.5, (b) co = 1, (c) co = 1.5, and (d) co = 2. Various colors mark the different values with diverse frequency points and θ_s. The solid black lines enclose the regimes of the absorptivity greater than 0.9.

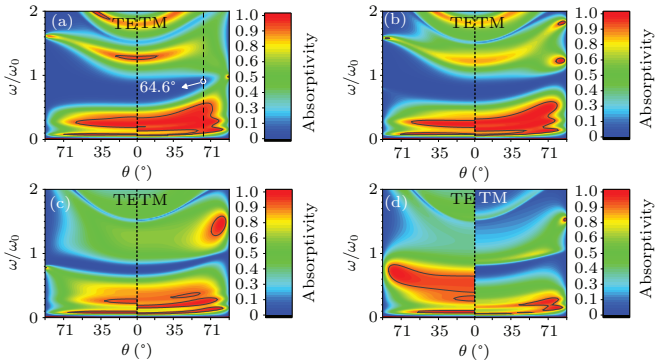

Fig. 11. Contour maps illustrating the ABs for the negative propagation with the defect located between different interlayers. The structures of the MGPCs are in the form of (a) $[(G_1C_1IY)^{N_1}\ (YC_2G_2)^{N_2}\ (C_2G_3\ G_4)^{N_3}]$, (b) $[(G_1C_1IY)^{N_1}\ (YC_2G_2)^{N_2-1}\ YC_2\ (C_2G_3\ G_4)^{N_3}\ G_2]$, (c) $[(G_1C_1IY)^{N_1}\ (YC_2G_2)^{N_2-1}\ Y(C_2G_3\ G_4)^{N_3}C_2\ G_2]$, (d) $[(G_1C_1IY)^{N1}\ (YC_2G_2)^{N_2-1}\ (C_2G_3\ G_4)^{N_3}(YC_2\ G_2)]$.

However, the AB of the TE wave expands to 0.18ω. In addition, in the TM wave regime of the AB, there is a narrow frequency band at 0.2ω, over which the absorptivity is less than 0.9. It covers the angular range from 0° to 7.8°. Moreover, in the case of $[(G_1C_1IY)^{N_1}\ (YC_2G_2)^{N_2}\ (C_2G_3\ G_4)^{N_3}]$, the defect filter does not operate well, when the TM waves are incident at a large angle, in the high frequency range around 0.9ω. As denoted in Fig. 11(a), the absorptivity is more than 0.1 in the case of θ more than 64.6°. However, in Fig. 11(b) over the corresponding frequency band, the absorptivity maintains less than 0.1, regardless of the incident angle. With respect to $[(G_1C_1IY)^{N_1}\ (YC_2G_2)^{N_2-1}\ Y(C_2G_3\ G_4)^{N_3}C_2\ G_2]$ in Fig. 11(c), the main AB is weakened, but the narrow AB in the low frequency band remains. In the TE wave regime, the AB covers the angular range from 0° to 66.2°, while in the TM wave regime, the AB reaches 82.4°. In Fig. 11(d), the ABs in the TE and TM wave regime vary. It can be attributed to the different optical properties of the Y layers under the TE and TM waves. The wide-angle AB in the TE wave regime shifts to the higher frequency range. In the case of normal incidence, the lower and upper edges of the AB are 0.4ω and 0.66ω, respectively. Also, the AB ranges from 0° to 83° in the angular range.

4. Conclusion

In summary, the MGPCs, having the property of the nonreciprocal wide-angle bidirectional absorption, are designed in the study. H, T_0, and B are taken as 10000 Oe, 295 K, and 1 T. In the studied domain, the EM waves are either absorbed or reflected and the ABs for the positive and negative propagation are perfectly staggered. The absorption for the positive propagation is based on the OTS. At $\theta = 0°$, the widths of the frequency ranges for both the TE and TM waves reach the peaks, covering a width of 0.22ω and 0.16ω, respectively. For the TE waves, the ABs in the angular range reach as far as 60°, while it attains 51° as to the TM waves. When it comes to the ABs for the negative propagation, the ABs can be attributed to the coherent subtraction in the resonant cavities. For the TE waves, the ABs take coverage of 0.11ω at its maximum at $\theta = 0°$ and extend horizontally to $\theta = 60°$ in the angular range. With respect to the TM waves, the ABs hold the frequency range of 0.46ω at 62°, which is the widest of the range. For the negative propagation, there is an additional narrow AB in the low frequency, localized in the interval between 0.06ω and 0.1ω. The introduced defect in the $MGPC_2$ works like a filter, which enhances the absorption in the low-frequency range around 0.25ω and blocks the EM waves around 0.8ω. T, H, n_{G_1}, and d_f are adjusted to investigate the effects on the ABs. It turns out that decreasing T_0 shrinks the ABs for the positive propagation in the scale of the angular range and expands them in the frequency range. H makes a difference to the ABs for the negative propagation. In the case of $H = 100$ Oe and TE waves, the ABs for the negative propagation expand to 0.18ω at $\theta = 0°$. Noticeably, n_{G_1} and d_f play significant roles on the ABs for the positive and the negative propagation, respectively. In the TE wave regimes, $n_{G_1} = 2$ localizes the ABs in a narrow angular range between $\theta = 47.8°$ and $\theta = 81.8°$. In addition, the higher the value of d_f, the narrower the ABs in the frequency band tend to be. This work provides an approach to isolators. However, how to better enhance insensitivity in the angular range and expand the frequency band remains to be studied.

Acknowledgement

Project supported by the College Student Innovation Training Program of Nanjing University of Posts and Telecommunications, and the Jiangsu Agriculture Science and Technology Innovation Fund (JASTIF) (Grant No. CX(21)3187).

References

[1] Yablonovitch E 1987 *Phys. Rev. Lett* **58** 2059
[2] John S 1987 *Phys. Rev. Lett.* **58** 2486
[3] Potton R J 2004 *Rep. Prog. Phys.* **67** 717
[4] Kato H, Matsushita T, Takayama A, Egawa M, Nishimura K and Inoue M 2002 *IEEE Trans. Magn.* **38** 3246

[5] Zhang L, Yang D, Chen K, Li T and Xia S 2013 *Opt. Laser Technol.* **50** 195
[6] Wang Z Y, Yu Z H, Zheng X D and Wang L 2012 *J. Electromagnet. Waves Appl.* **26** 1476
[7] Fu W, Shu F J, Zhang Y L, Dong C H, Zou C L and Guo G C 2015 *Opt. Express* **23** 25118
[8] Xue C, Jiang H and Chen H 2010 *Opt. Express* **18** 7479
[9] Hu X, Li Z, Zhang J, Yang H, Gong Q and Zhang X 2011 *Adv. Funct.* **21** 1803
[10] Gevorgyan A H, Golik S S and Gevorgyan T A 2019 *J. Magn. Magn. Mater.* **474** 173
[11] Smith K and Chabanov A A 2011 *Integr. Ferroelectr.* **131** 66
[12] Ardakani A G 2014 *J. Opt. Soc. Am. B* **31** 332
[13] Zamani M, Amanollahi M and Taraz M 2019 *Opt. Mater.* **88** 187
[14] Kalish A N, Komarov R S, Kozhaev M A, Achanta V G, Dagesyan S A, Shaposhnikov A N and Belotelov V I 2018 *Optica* **5** 617
[15] Liu K, Shen L and He S 2012 *Opt. Lett.* **37** 4110
[16] Yang Y, Poo Y, Wu R X, Gu Y and Chen P 2013 *Appl. Phys. Lett.* **102** 231113
[17] Yu G X, Fu J J, Du W W, Lv Y H and Luo M 2019 *Chin. Phys. B* **28** 024101
[18] Du G X, Mori T, Suzuki M, Saito S, Fukuda H and Takahashi M 2010 *Appl. Phys. Lett.* **96** 081915
[19] Ardakani A G 2014 *J. Opt. Soc. Am. B* **31** 332
[20] Yu G, Zhang X, Lv Y and Cao R 2021 *Optik* **248** 166230
[21] Hu S, Song J, Guo Z, Jiang H, Deng F, Dong L and Chen H 2022 *Opt. Express* **30** 12104
[22] Schurig D, Mock J J, Justice B J, Cummer S A, Pendry J B, Starr A F and Smith D R 2006 *Science* **314** 977
[23] Shameli M A and Yousefi L 2022 *Opt. Laser Technol.* **145** 107457
[24] Parmar J and Patel S K 2022 *Physica B* **624** 413399
[25] Li Z, Palacios E, Butun S, Kocer H and Aydin K 2015 *Sci. Rep.* **5** 15137
[26] Li H, Qin M, Wang L, Zhai X, Ren R and Hu J 2017 *Opt. Express* **25** 31612
[27] Xu Z B, Qi Z H, Wang G W, Liu C, Cui J H, Li W L and Wang T 2022 *Chin. Phys. B* **31** 087504
[28] Dasgupta B, Dasgupta P, Janaki M S, Watanabe T and Sato T 1998 *Phys. Rev. Lett.* **81** 3144
[29] Wu F, Wu X, Xiao S, Liu G and Li H 2021 *Opt. Express* **29** 23976
[30] Su Z P, Wei T T and Wang Y K 2022 *Chin. Phys. B* **31** 087804
[31] Qi L M, Yang Z Q, Lan F, Gao X and Shi Z J 2010 *Phys. Plasmas* **17** 042501
[32] Wang H and Li Y P 2001 *Acta Phys. Sin.* **50** 2172 (in Chinese)
[33] Sharma Y, Prasad S and Singh V 2018 *Opt. Quantum Electron.* **50** 1
[34] Mehdian H, Mohammadzahery Z and Hasanbeigi A 2015 *J. Phys. D: Appl. Phys.* **48** 305101
[35] Dai X, Xiang Y, Wen S and He H 2011 *J. Phys. D: Appl. Phys.* **109** 053104
[36] Chen S, Fan F, Wang X, Wu P, Zhang H and Chang S 2015 *Opt. Express* **23** 1015
[37] Razi S and Ghasemi F 2019 *Chin. Phys. B* **28** 124205
[38] Chang T, Huang C, Hou D J, Wu C and Chen D 2017 *IEEE Photon. J.* **9** 5900509